

Dynamical stability for dense patterns in discrete attractor neural networks

Uri Cohen^{1,*} and Máté Lengyel^{1,2}

¹*Computational and Biological Learning Lab, Dept. of Engineering,
University of Cambridge, Cambridge, UK*

²*Center for Cognitive Computation, Department of Cognitive Science,
Central European University, Budapest, Hungary*

Neural networks storing multiple discrete attractors are canonical models of biological memory. Previously, the dynamical stability of such networks could only be guaranteed under highly restrictive conditions. Here, we derive a theory of the local stability of discrete fixed points in a broad class of networks with graded neural activities and in the presence of noise. By directly analyzing the bulk and the outliers of the Jacobian spectrum, we show that all fixed points are stable below a critical load that is distinct from the classical *critical capacity* and depends on the statistics of neural activities in the fixed points as well as the single-neuron activation function. Our analysis highlights the computational benefits of threshold-linear activation and sparse-like patterns.

Introduction. Attractor neural networks are canonical models of biological memory: they store neural activity patterns as stable fixed points (i.e., attractors) in their connection weights, so that when started from a noisy or incomplete version of one of these memory patterns as an initial condition, their autonomous dynamics converge to the corresponding fixed point owing to its dynamical stability – thus performing ‘auto-associative’ memory recall [1, 2]. Therefore, the stability of memory patterns as fixed points is critical for the operation of attractor networks. However, previous approaches had limited success in studying fixed-point stability.

The ‘Hebbian’ approach guarantees fixed-point stability in attractor networks by constructing an energy (or Lyapunov) function that is minimized by the network dynamics [1]. However, this has only been possible in a few (albeit very successful) cases [3–7] after making specific assumptions about the statistics of memory patterns (typically assumed to be binary), single-neuron activation functions (saturating, or rectified-linear), and in particular the way memory patterns influence dynamics (through some form of a so-called ‘Hebbian’ learning rule) requiring normal connection weight matrices. Even when those assumptions were violated, stability was achieved by approximately following such an energy function [8–10]. Conversely, the ‘Gardner’ approach allows the analysis of the storage capacity of neural networks in terms of the number of fixed points that can be embedded in their dynamics without recourse to an energy function [11, 12], but remains entirely mute about the stability of the embedded fixed points. Finally, optimization-based numerical approaches have also been used to embed stable fixed points in neural networks without making limiting assumptions, but they did not lend themselves to theoretical insight [13].

In this letter, we extend the ‘Gardner’ approach to gain analytical insights about the stability of fixed points in a broad class of networks with graded neural activities and generic, non-saturating, rectified, power-law activa-

tion functions. In particular, rather than the oft-studied sparse limit, here we consider dense patterns for analytical tractability on dynamical stability, and also because the inherent noisiness of neural signaling can easily prevent firing rates from being exactly zero in practice. To supplement these analyses, we also consider sparse patterns (Fig. S1a) and show that our results extend to those in numerical simulations. We demonstrate that there is a phase transition for stability in such networks: optimizing network connectivity to maintain memory patterns as fixed points with minimal weights renders either all or none of those fixed points stable, depending on pattern statistics and single-neuron properties. By characterizing the conditions under which fixed-point stability emerges in a large class of network dynamics, we provide design principles for biological systems performing auto-associative memory [14, 15].

Network model for auto-associative memory. We study a network of N neurons with voltage dynamics:

$$\tau \dot{\mathbf{v}} = -\mathbf{v} + \mathbf{W} \mathbf{g}(\mathbf{v} - \boldsymbol{\theta}) \quad (1)$$

where v_i is the voltage of neuron i , τ is the neural time constant, $\mathbf{W} \in \mathbb{R}^{N \times N}$ defines recurrent connection weights (such that W_{ij} is the strength of the connection from neuron j to neuron i), $g_i(\mathbf{v}) = g(v_i) : \mathbb{R} \rightarrow \mathbb{R}^+$ is the neural activation function that maps the ‘voltage’ of a neuron, v_i , to its (positive) instantaneous firing rate, and $\theta_i = \theta \in \mathbb{R}$ is the ‘threshold’ (or negative bias) for neuron i . (Note that τ , $g(\cdot)$, and θ are shared across neurons.) Defining $\mathbf{v} = \mathbf{W} \mathbf{r}$, Eq. 1 has an equivalent form of rate dynamics [16], which is the form we will use in the following for mathematical convenience:

$$\tau \dot{\mathbf{r}} = -\mathbf{r} + \mathbf{g}(\mathbf{W} \mathbf{r} - \boldsymbol{\theta}) \quad (2)$$

While our theoretical results hold for a wide range of activation functions $g(\cdot)$, with additional assumptions detailed below, we consider here the specific case of the

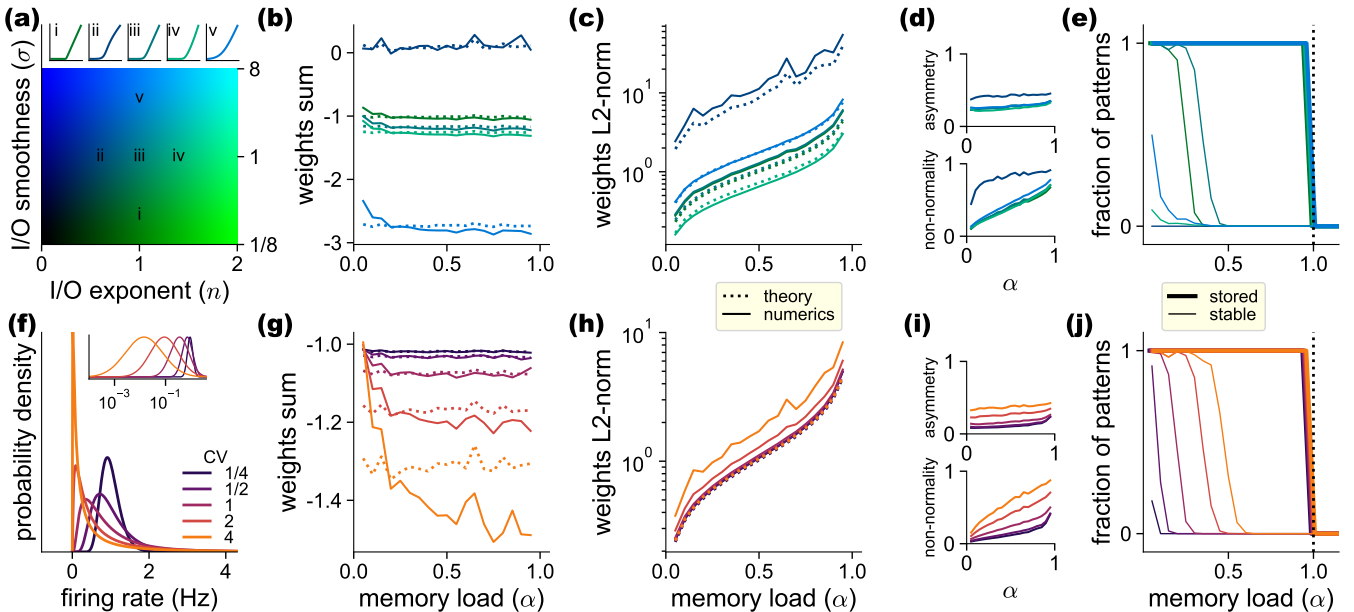


FIG. 1. **Storing fixed-points.** (a) Color code for combinations of I/O exponent (x-axis) and smoothness (y-axis, log-scale). The activation function for selected combinations is illustrated (insets, top). These combinations are used in b-e, with $CV = 2, \theta = -2$. (b,c) The sum (b) and L2-norm (c) of the presynaptic weights of a neuron (i.e. a row of \mathbf{W}) as a function of memory load (α) for different activation functions (colors as in a). Note the divergence of L2-norm as $\alpha \rightarrow 1$, as predicted by theory. (d) Measures of the weights asymmetry (top) and dynamics non-normality (bottom) at different load values (x-axis), for different activation functions (colors as in a). (e) The fraction of patterns which are correctly stored (thick curves) or stable for recall (thin curves) as a function of memory load (α) for different activation functions (colors as in a). (f) Probability density of log-normal distributed patterns at different values of CV (color coded). The inset shows normalized density on a log scale. (g-j) Same as b-e for different values of pattern CV (colors as in f) with $\sigma = 1, n = 1, \theta = -2$. Solid vs. dotted lines in b,c,e, and g,h,i show numerical vs. theoretical results (with only numerical results shown for stability e,j – see subsequent figures for corresponding theoretical results). Numerical simulations optimized the weights \mathbf{W} according to Eq. 4 at $N = 256$.

soft-rectified power-law to be able to systematically study how stability depends on its parameters (Fig. 1a):

$$g(v) = \left[\frac{\sigma}{\pi} \ln(1 + e^{\frac{\pi}{\sigma} v}) \right]^n \quad (3)$$

with exponent n and smoothness σ . The particular form of Eq. 3 is motivated as an approximation to a hard-rectified power-law activation function acting on noisy voltages, where voltage noise is Gaussian with standard deviation σ : $g(v) = \langle |v + \sigma z|_+^n \rangle_{z \sim \mathcal{N}(0,1)}$. Note that due to the noisiness of the activation function (or the equivalent smoothness in Eq. 3), all patterns in the network are dense as firing rates are never exactly zero. We also present results for a noiseless rectified power-law activation function that gives rise to sparse patterns (Details).

In line with previous approaches [11, 12], we begin by formalising the computational task for an auto-associative memory as the following: given a set of P memory patterns \mathbf{r}^μ for $\mu = 1 \dots P$, find minimal-norm weights such that each memory pattern is a fixed-point of the network dynamics (Eq. 2):

$$\begin{aligned} \mathbf{W}^* = \operatorname{argmin}_{\mathbf{W}} \|\mathbf{W}\|_F \\ \text{s.t. } \mathbf{r}^\mu = \mathbf{g}(\mathbf{W} \mathbf{r}^\mu - \boldsymbol{\theta}) \quad \forall \mu = 1 \dots P \end{aligned} \quad (4)$$

We consider the additional constraint that there are no self-couplings, i.e. the diagonal elements of the connection weight matrix are zero.

We deviate from previous approaches [1, 2, 5, 12] in two important ways. First, we not only require memory patterns to be merely fixed points of the dynamics (which will be guaranteed once Eq. 4 is solved), but we also study the local stability of these fixed points – this is critical for a well-functioning auto-associative memory if it is to perform memory recall by converging to a memory pattern when started from a state that is near but not identical to it [1, 17]. Specifically, we analyze the Jacobian of the dynamics around each memory pattern

$$\mathbf{J}_\mu = -\mathbf{I} + \mathbf{g}'(\mathbf{g}^{-1}(\mathbf{r}^\mu)) \circ \mathbf{W} \quad (5)$$

The fixed-point at \mathbf{r}^μ is stable if all eigenvalues of the Jacobian have negative real parts.

Second, unlike previous approaches that considered binary [1, 2] or sparse memory patterns [5, 12], here we specifically focus on dense patterns in which firing rates are never exactly zero: $\mathbf{r}^\mu \in \mathbf{R}_+^N$. Again, to allow a systematic study of how stability depends on the properties of this distribution, we consider here

the specific case of a log-normal distribution of patterns, which we parametrize by its coefficient of variation $CV = \sqrt{\langle \delta r^2 \rangle / \langle r \rangle}$, while fixing its mean at $\langle r \rangle = 1$ (Fig. 1f), where here and in the following $\langle \cdot \rangle$ and δ denote averaging across the distribution of memory patterns and computing the deviation from such an average, respectively. For a hard-rectified power law activation function (i.e. $\sigma = 0$, Fig. S1b), scaling the mean of memory patterns while keeping their CV constant would cancel in the Jacobian of the dynamics, Eq. 5, thus leaving stability unaffected. For our soft-rectified activation function, this does not hold exactly, but we find the effects on stability to be negligible, Fig. S4. While such patterns are always technically dense, they can approximate sparse distributions with a sufficiently high CV (we call such patterns ‘sparse-like’).

To summarize, we are interested in how the maximal number of patterns P that can be stored as fixed points, and the fraction of these fixed points that are dynamically stable, depend on parameters σ , n , θ , and CV (as well as f , the sparseness of patterns, Details). For obtaining this maximum, we optimize \mathbf{W} following Eq. 4.

Mean-field theory for storage capacity. A replica analysis of the solution for the optimization problem Eq. 4 follows the Gardner approach [11, 12, 18], without assuming specific connection weights as in the Hopfield model [2, 5]. In the Appendix, we derive a mean-field theory for the capacity to store graded, random memory patterns as fixed points of Eq. 1, without assumptions on the weights. The analysis applies to either dense patterns with a strictly monotonic activation function or to sparse patterns with a rectified monotonic activation function. It generalizes previous work in which a rectified-linear activation function and normalized connection weights were assumed [12]. As usual, our analysis assumes $P, N \rightarrow \infty$ with a fixed memory load $\alpha = P/N$ and uses the replica technique, assuming the replica symmetry ansatz [19].

In line with previous results [11], our theory predicts that there is a critical capacity α_C , such that as α approaches α_C , there is no longer a solution to Eq. 4. We find that α_C depends only on pattern sparseness (Details, Fig. S1g) and is independent of other pattern statistics (CV; Fig. 1f), neural thresholds (θ ; Eq. 2, Fig. S3a), and activation function details (smoothness σ and exponent n ; Eq. 3, Fig. 1a), thus extending results from neurons with binary [4, 11] or rectified-linear activation functions (corresponding to $\sigma = 0$, $n = 1$) to our broader class of activation functions ($\sigma \geq 0$, $n > 0$) [12]. Results for the sparse case are presented in Fig. S1 (Details). In the dense case, the critical capacity is $\alpha_C = 1$ (again, independent from any of the parameters), and theory predicts the following moments for each element of the connection

weight matrix:

$$N \langle W^2 \rangle = \frac{\alpha}{1 - \alpha} \frac{\langle \delta g^{-1}(r)^2 \rangle}{\langle \delta r^2 \rangle} \quad (6)$$

$$N \langle W \rangle = \frac{\theta + \langle g^{-1}(r) \rangle}{\langle r \rangle} \quad (7)$$

For a subcritical load, $\alpha = P/N < \alpha_C$, theory can be compared with numerical experiments by directly solving Eq. 4 using off-the-shelf optimizers [20]. The theory provides a good match for both the mean ($N \langle W \rangle$) from Eq. 7; Fig. 1b,g, Fig. S1c, and Fig. S3b) and the L2-norm of a row of the connection weight matrix ($\sqrt{N \langle W^2 \rangle}$ from Eq. 6; Fig. 1c,h, Fig. S1d, and Fig. S3c). As α approaches α_C , the theory predicts the L2-norm of weights to diverge, explaining why there is no solution to Eq. 4 in this regime (Fig. 1e,j, Fig. S1e,f, and Fig. S3e).

To test if the resulting dynamics might coincide with those assumed by the ‘Hebbian’ approach, we measured the weight matrix asymmetry and the deviation from normality of the dynamics around the fixed points (Details). Both are non-negligible and increase with the problem’s load α and pattern variation (Fig. 1d,i, and Fig. S3d), indicating the resulting dynamics are distinct from those of energy-based models.

Importantly, investigating the emergent stability of patterns in the subcritical regime reveals a second phase transition: all patterns tend to be stable up to a new critical value $\alpha_S < \alpha_C$, above which all patterns tend to be unstable (Fig. 1e,j, Fig. S2a,b, and Fig. S3e). In the following, we investigate this phenomenon more closely.

Theory of stability for dense patterns. For dense patterns, $\alpha_C = 1$ and for any $\alpha < \alpha_C$ the solution to Eq. 4 is given in closed-form (Details):

$$\mathbf{W}^* = \mathbf{V} \mathbf{R}^\dagger = \mathbf{V} (\mathbf{R}^\top \mathbf{R})^{-1} \mathbf{R}^\top \quad (8)$$

where $\mathbf{R}, \mathbf{V} \in \mathbb{R}^{N \times P}$ are the stored memory patterns $R_{i\mu} = r_i^\mu$ and $V_{i\mu} = g^{-1}(R_{i\mu}) + \theta$. A slightly more complicated expression is available when avoiding self-couplings, Eq. 19, but we find that we can neglect this difference and use Eq. 8 in the derivation of stability. This generalizes earlier results derived for storing binary patterns, in which case weights defined through the patterns’ pseudo-inverse were already proposed in the ‘Hebbian’ approach [3, 21]. However, those results were limited to a linear activation function $\mathbf{V} = \mathbf{R}$, rendering \mathbf{W} symmetric (and thus allowing the construction of an energy function). In the general case of a non-linear activation function, \mathbf{W}^* obtained from Eq. 8 is not symmetric and thus falls outside the scope of the ‘Hebbian’ approach.

To characterize α_S , the critical load for the stability of \mathbf{J}_μ with $\mathbf{W} = \mathbf{W}^*$, we note that from Eqs. 5 and 8:

$$\mathbf{J}_\mu^* = -\mathbf{I} + \underbrace{\mathbf{g}'(\mathbf{g}^{-1}(\mathbf{r}^\mu)) \circ \mathbf{V} \mathbf{R}^\dagger}_{\mathbf{V}_\mu} \quad (9)$$

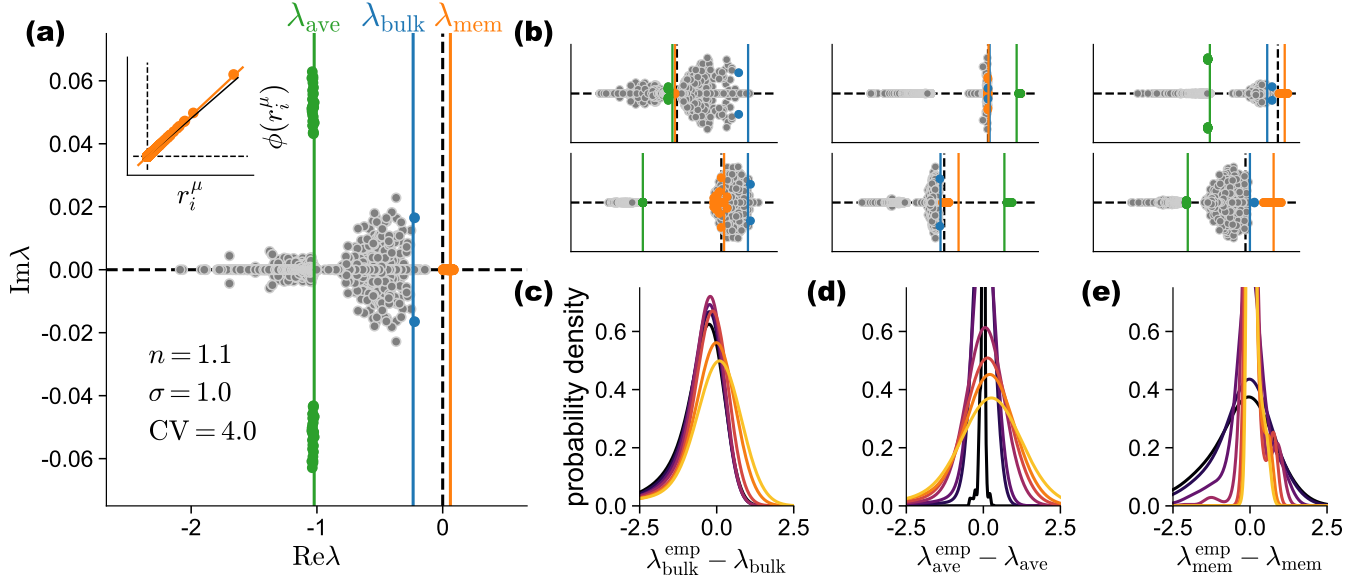


FIG. 2. **Fixed-point stability.** (a) Example spectrum - overlaid eigenvalues of P Jacobians \mathbf{J}_μ of a single problem (parameters indicated by text). Annotations of the theoretical values λ_{bulk} (blue line), λ_{ave} (green line), and λ_{mem} (orange line). The corresponding empirical eigenvalues are marked with matching colors: largest eigenvalue of the bulk (blue dot), the eigenvalue associated with the Jacobian average (green dot), and the eigenvalue associated with the memory pattern (orange dot). Inset shows a near-linear relation between r_i^μ (x-axis) and $\phi(r_i^\mu)$ (y-axis), a prerequisite for an outlier λ_{mem} . (b) Same as a, for six parameter sets; columns differ by the maximal theoretical value. (c-e) Probability densities at different CV values (color-coded) of the difference between the empirical and predicted value of λ_{bulk} (c), λ_{ave} (d), and λ_{mem} (e), calculated over different choice of the parameters discussed in Figs. 1 and S3, in cases where $|\lambda_{\text{bulk}}| < 10$ (c), $|\lambda_{\text{ave}}| < 10$ (d), $\tau_{\text{mem}} > 0.95$ (e).

and build on our previous analysis of the eigenvalue spectrum of random matrices $\mathbf{M} = -\mathbf{I} + \mathbf{X}\mathbf{Y}^\dagger$ when pairs of the corresponding entries of \mathbf{X} and \mathbf{Y} are (jointly) independent and identically distributed (i.i.d.), correlated Gaussian, and α simply denotes the dimension-ratio (width/height) of \mathbf{X} and \mathbf{Y} (a generalization of α being the load in our case) [22]. This analysis provides an exact result for the support of the eigenvalue spectrum (Fig. S5) and the largest real eigenvalue λ_{bulk} of \mathbf{M} (Details, Eq. 21). Interestingly, we find that, just as the Jacobians of the original network, \mathbf{J}_μ^* , the Jacobians defined by \mathbf{M} (for any choice of \mathbf{X} and \mathbf{Y}) also undergo a phase transition: they are either all stable (for $\alpha < \alpha_S$) or all unstable (for $\alpha > \alpha_S$) (Details, Eq. 22). To apply the general theory of the eigenvalue spectrum of \mathbf{M} to the eigenvalue spectrum of \mathbf{J}_μ^* (Eq. 9), we choose \mathbf{X} and \mathbf{Y} such that the variances and covariance of $X_{i\mu}$ and $Y_{i\mu}$ are respectively $c_{\text{ff}} = \langle \delta f(r, r')^2 \rangle$, $c_{\text{rr}} = \langle \delta r^2 \rangle$, and $c_{\text{rf}} = \langle \delta r \delta f(r, r') \rangle$, where $f(r, r') = g'(g^{-1}(r'))(g^{-1}(r) + \theta)$ for independent variables r, r' . With these substitutions,

$$\lambda_{\text{bulk}} = -1 + \frac{c_{\text{rf}}}{c_{\text{rr}}} + \frac{1}{c_{\text{rr}}} \sqrt{\frac{\alpha}{1-\alpha} (c_{\text{rr}} c_{\text{ff}} - c_{\text{rf}}^2)} \quad (10)$$

Solving for the largest value of α for which $\lambda_{\text{bulk}} < 0$, the resulting critical load for stability from this analysis is:

$$\alpha_S^{\text{bulk}} = \frac{\max(0, c_{\text{rr}} - c_{\text{rf}})^2}{c_{\text{rr}} c_{\text{ff}} - c_{\text{rf}}^2 + (c_{\text{rr}} - c_{\text{rf}})^2} \quad (11)$$

The foregoing stability analysis was based on the zero-crossing of the ‘rightmost point’ of the bulk of the eigenvalue spectrum of \mathbf{M} , λ_{bulk} . However, we note that this eigenvalue spectrum can only be an approximation to that of \mathbf{J}_μ^* (Fig. 2a), since the entries of \mathbf{J}_μ^* are neither i.i.d. (due to the $g'(g^{-1}(r'))$ term in $\bar{\mathbf{V}}_\mu$, which couples different rows), nor Gaussian (since \mathbf{V} is a deterministic function of \mathbf{R} , rather than being a jointly distributed random variable). Despite these facts, we empirically find that the eigenvalue spectrum of \mathbf{M} often provides an acceptable approximation to at least the bulk of the eigenvalue spectrum of \mathbf{J}_μ^* , so that λ_{bulk} often predicts stability well (Fig. 2a,c and Fig. 2b, left column). Nevertheless, there are also cases when λ_{bulk} alone is an imperfect predictor of stability (Fig. 2b, middle and right columns). Thus, we analyze two specific outlier eigenvalues that might interfere with stability.

The analysis of each of the two outlier eigenvalues is based on assuming the existence of a specific eigenvector of \mathbf{J}_μ^* and computing its corresponding eigenvalue, which may be an outlier. In the first case, we make the assumption that the uniform vector, $\mathbf{1}$, is an eigenvector. If such an eigenvector existed, the corresponding eigenvalue, λ_{ave}^μ , would be the (average) row-sum of \mathbf{J}_μ^* , \bar{J} . Thus, using replica theory (Eq. 7) to compute $N\langle W \rangle$,

the expectation of this outlier eigenvalue is:

$$\lambda_{\text{ave}} = \langle \lambda_{\text{ave}}^\mu \rangle = \langle \bar{J} \rangle = -1 + \langle g'(g^{-1}(r)) \rangle \frac{\theta + \langle g^{-1}(r) \rangle}{\langle r \rangle} \quad (12)$$

where by taking the expectation over $g'(g^{-1}(\mathbf{r}^\mu))$, we have again ignored its memory pattern-dependence. Even though the uniform vector is not an eigenvector of \mathbf{J}_μ^* in general, when we empirically identify the closest eigenvector (Details), we find that the associated eigenvalue is often close to λ_{ave} (Fig. 2a,d), and can determine the dynamical stability of \mathbf{J}_μ^* (Fig. 2b, middle column).

In the second case, we assume that there exists some constant c for which $\mathbf{r}^\mu + c \mathbf{1}$ is an eigenvector of \mathbf{J}_μ^* . In this case, the following equation must hold (Details):

$$\phi(\mathbf{r}^\mu) = (\lambda_{\text{mem}}^\mu + 1) \mathbf{r}^\mu + c (\lambda_{\text{mem}}^\mu - \lambda_{\text{ave}}) \mathbf{1} \quad (13)$$

where $\phi_i(\mathbf{r}) = \phi(r_i) = f(r_i, r_i)$. In practice, Eq. 13 may not hold exactly, so more generally we can characterize the (approximately) linear relationship between \mathbf{r}^μ and $\phi(\mathbf{r}^\mu)$ by the expectation of its correlation coefficient, τ_{mem}^μ , and slope, λ_{mem}^μ :

$$\tau_{\text{mem}} = \langle \tau_{\text{mem}}^\mu \rangle = c_{r\phi} / \sqrt{c_{rr} c_{\phi\phi}} \quad (14)$$

$$\lambda_{\text{mem}} = \langle \lambda_{\text{mem}}^\mu \rangle = -1 + c_{r\phi} / c_{rr} \quad (15)$$

where $c_{r\phi} = \langle \delta r \delta \phi(r) \rangle$, $c_{\phi\phi} = \langle \delta \phi(r)^2 \rangle$ are additional (co)variance terms, and the assumption on which the analysis of λ_{mem} is based can be expressed as $\tau_{\text{mem}} \approx 1$. To empirically test the relevance of λ_{mem}^μ (Eq. 15) for determining the stability of \mathbf{J}_μ^* , it is straightforward to identify the eigenvector of \mathbf{J}_μ^* associated with the highest τ_{mem}^μ , and compare the corresponding eigenvalue to λ_{mem} (Fig. 2a,e). Indeed, we find cases where λ_{mem}^μ determines the dynamical stability of \mathbf{J}_μ^* (Fig. 2b, right column).

For characterizing the transition from the stable to the unstable regime, we analyze the case when exactly half of the patterns stored in a network are stable. This means that we focus on the median λ_{ave}^μ and λ_{mem}^μ across patterns. As the expected value of this median is the expectation of an individual such eigenvalue, stability is determined by the zero crossings of the expectations we computed above (Eqs. 12 and 15). As neither of these expectations depend on the number of stored patterns, we can estimate the critical load for stability as:

$$\alpha_S = \alpha_S^{\text{bulk}} \Theta(-\lambda_{\text{ave}}) [1 - \Theta(\lambda_{\text{mem}}) \Theta(\tau_{\text{mem}} - 0.95)] \quad (16)$$

where $\tau_{\text{mem}} > 0.95$ is an arbitrary choice for the domain where we consider the prediction about λ_{mem} to apply.

We first focus on the zero crossing of α_S as a function of the parameters, i.e. the parameter regime where stability is possible at all. For this, we analyze the zero crossing of each of the three terms of Eq. 16 separately by solving the corresponding inequalities: $\alpha_S^{\text{bulk}} > 0$, $\lambda_{\text{ave}} < 0$, and

$\lambda_{\text{mem}} < 0$ (assuming $\tau_{\text{mem}} > 0.95$). The dependence of each of these zero crossings on θ is relatively straightforward. The zero crossing of α_S^{bulk} does not depend on θ (although the exact value of α_S^{bulk} when it is greater than zero does, Details). Both λ_{ave} and λ_{mem} depend on θ linearly (Eq. 12, and Details), and so the condition for their zero crossing can be expressed respectively as

$$\theta_0^{\text{ave}} = \frac{\langle r \rangle}{\langle d(r) \rangle} - \langle g^{-1}(r) \rangle \quad (17)$$

$$\text{and } \theta_0^{\text{mem}} = \frac{\langle \delta r \delta r \rangle - \langle \delta r \delta d(r) g^{-1}(r) \rangle}{\langle \delta r \delta d(r) \rangle} \quad (18)$$

where $d(r) = g'(g^{-1}(r))$, and the RHSs of Eqs. 17 and 18 implicitly depend on the other parameters (Details).

Phase diagrams. In order to gain insights into the complex dependence of the zero crossings of the three terms of Eq. 16 on the combination of parameters (pattern statistics CV, activation function smoothness σ , exponent n , and threshold θ), we solved the corresponding equations systematically over a range of parameter combinations, and compared these predictions with numerically obtained values of α_S . Fig. 3a presents the resulting phase diagrams of α_S for different pairs of parameters when the third parameter is kept fixed, showing where α_S^{bulk} , λ_{ave} , and λ_{mem} (the three main determinants of α_S according to Eq. 16) are predicted to cross zero (blue, green, and orange lines, respectively) as well as the numerically computed values of α_S (grayscale map). We note that λ_{ave} constrains stability only for $\theta > 1, n \approx 1$ (Fig. 3a middle panel), while the upper bound on the threshold θ is due to the zero crossing of λ_{mem} (Eq. 18). The superior stability near $n = 1$ is explained by noting that while λ_{bulk} prevents stability at most of the sublinear regime, where $c_{rf} \geq c_{rr}$, λ_{mem} prevents stability at most of the supralinear regime, where $c_{r\phi} \geq c_{rr}$. Interestingly, the former is derived by neglecting the pattern-specific statistical dependency between the rows of the Jacobian, while the latter is a result of this dependency.

Furthermore, we can now better understand the limitations of the theory: the zero crossing of λ_{mem} yields a discontinuous fall of α_S from a finite value to 0 (Eq. 16), and in many cases the maxima is achieved at this boundary. Thus, deviations of the empirical value of this outlier would cause large prediction errors in that boundary. Furthermore, in two regimes – large σ and low θ – we observe regions where the assumption on the memory-pattern related outlier is violated, and the empirical value of the outlier is larger than theory predicts, so the empirical α_S might be zero while theory predicts otherwise.

To complement these results, Fig. 3b presents similar phase diagrams, but where the third parameter is optimized for each pair of systematically varied parameters, rather than kept fixed. The results remain qualitatively similar to those obtained above (Fig. 3a). This view highlights the superiority of $n = 1$ and $\sigma = 1$ in terms of the

resulting number of stable memories, which is further demonstrated across all CV values in Fig. 3c-d for n and σ , respectively. On the other hand, the effect of θ seems minor, as long as it is below an upper bound.

Optimal parameters. Fig. S4 presents the maximal achievable value for the stability critical load as a function of pattern statistics, as well as the optimal parameters where the optimum is achieved for various choices of $\langle r \rangle$. Our theory predicts improvement of stability with pattern variation (Fig. 3c-d, Fig. S4a). Those high-variance memory patterns are sparse-like, with many near-zero values and few large activations, so the improved capacity we report for those echoes the benefit of sparseness in our results (Fig. S2a,e) and previous works [4, 5]. Such sparse-like patterns are also consistent with the known phenomenology of neurons in the brain [23, 24]. As noted above, such patterns require highly asymmetric weights and lead to dynamics distinct from those of energy-based models (Fig. 1i).

Our analysis predicts substantial stability only in the near-linear region $n \approx 1$ (Fig. 3c, Fig. S4b). The benefits of threshold-linear activation are also observable for sparse patterns (Fig. S2e), where it is optimal for $CV \geq 1$. This is consistent with previous literature on storage of graded memory patterns using the ‘Hebbian’ approach, which focused on this activation function [5, 12] and with the machine learning literature using similar activations [25], but contrasts with other approaches that advocate for the benefits of supralinear activation [26, 27].

Numerical results demonstrate that the optimal choice of σ is a finite value (Fig. 3d, Fig. S4c). Theory does not predict this value well due to the abovementioned imprecisions in the estimation of the zero crossing of λ_{mem} .

In our analysis, the optimal threshold is negative. This is supported by the theory bounding the threshold from above (Fig. 3a-b), and is evident empirically at the optimal parameters for dense patterns (Fig. S4d), as well as for sparse patterns (Fig. S2c). A negative threshold implies that neurons are biased toward activity and are held back by recurrent connections which are dominated by inhibition (i.e. $m < 0$), as shown for the near-optimal values $n = 1, \sigma = 1$ at Fig. 1g. This contrasts with previous proposals for how recurrent neural networks can perform associative memory (a notable exception is the Willshaw network [28]) and with the prevailing view in the field [17], according to which the construction of multiple distinct and stable activity patterns requires global inhibition and selective recurrent excitation.

Discussion. Our analysis highlights the conditions for memory pattern stability in attractor networks performing auto-associative memory recall. The resulting theory makes several testable predictions, most notably a *stability phase transition* at a number of patterns which is proportional to the number of neurons, below the *capacity phase transition*, which does not account for stability. It

constrains the range of possible choices for single-neuron activation functions and establishes that near-linear activation, a negative threshold, and non-zero noise levels are optimal for the stable recall of dense memory patterns.

The predictions above are relevant to neuroscience and cannot be derived from the non-biological, energy-based auto-associative memory networks commonly used in the field. This letter paves the way for designing networks with biologically relevant dynamics capable of storing a large number of patterns as stable fixed points by standard optimization approaches. In particular, optimization only needs to consider the existence of fixed points, not their stability, as the latter is guaranteed under the stability phase transition. Future research will need to establish if biologically plausible local learning rules, rather than optimization, can achieve similar results.

Several areas of science study dynamical systems where fixed points and their dynamic stability may be of interest [29]. This question is analyzed theoretically, as in our case, through the eigenvalue spectrum of the dynamics’ Jacobian at fixed points. Full characterization of the spectrum is possible for a variety of random matrix ensembles [30–36] and exhibits a universality property [37]. Many random dynamical systems (whose local linearization induces a random matrix ensemble) exhibit a stability phase transition as some parameter of the ensemble is increased [29, 35, 38–40]. Such random dynamical systems can have an exponential number of fixed points, with stability that depends on a global criterion [34, 41, 42]. In this letter, we were able to go beyond random matrices (or low-rank perturbations thereof [43, 44]) to describe fixed-point stability in a system resulting from an optimization process, where the connection weight matrix (and subsequently the Jacobian) has considerable structure defined by the objective function it minimizes. The stability of fixed points in an optimized network was previously described analytically only for simple cases, when storing a single pattern of activity by optimizing the weights of a single feedback neuron (i.e. a rank-1 perturbation of the weights) [45], or a very small number of patterns using a rank-2 perturbation [46]. Our work provides conditions for the dynamical stability of networks optimized to store a large number of memory patterns.

Our analysis of the eigenvalue spectrum of the Jacobian may be applicable to many other systems where an optimal solution is given by a pseudo-inverse, as in multivariate linear regression problems $S^* = \arg \min_S \|A - BS\|_F$ for rectangular matrices A, B and a square matrix S . Those arise naturally in many areas of science, such as in the case of time series analysis where A and B are time-lagged ‘Trajectory Matrices’, useful for the analysis of non-linear dynamics (in ‘Singular Spectrum Analysis’ [47, 48]), for Multivariate Calibration in Chemometrics (in ‘Principal Component Regression’ [49]) and in the study of fluid dynamics (in ‘Dynamic Mode Decomposition’ [50]). Our approach, in particular deriving ex-

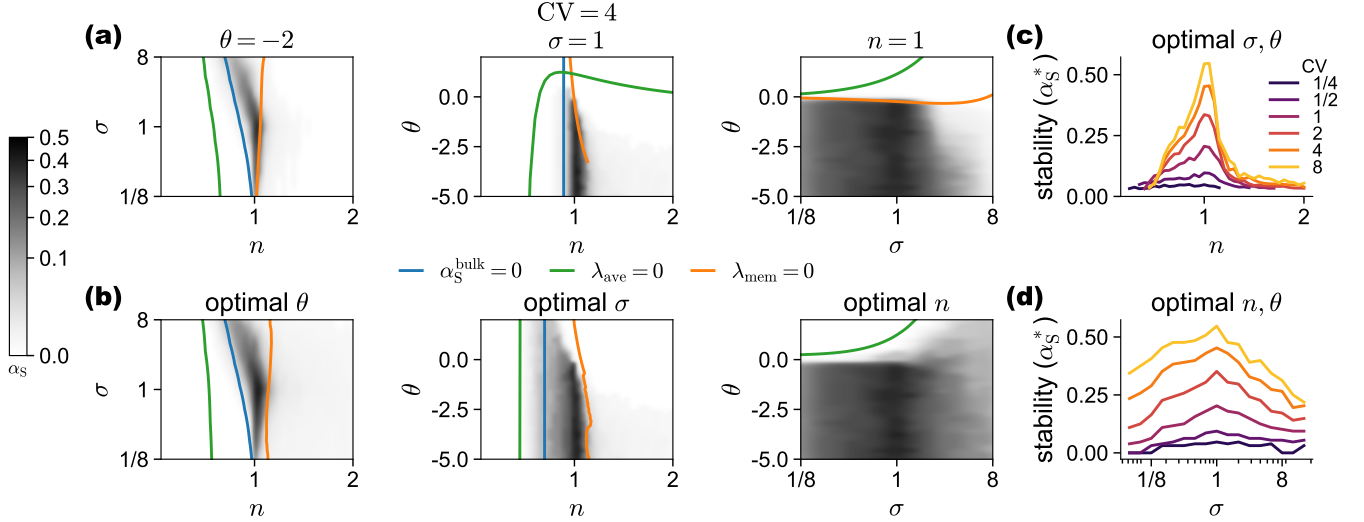


FIG. 3. **Phase diagrams for the critical load for stability.** (a-b) Numerical simulations results for the critical load for stability α_S (grayscale map) using different choices of I/O exponent n , smoothness σ , and threshold θ , and theoretical predictions for the zero-crossings of the different terms in Eq. 16, i.e. $\alpha_S^{\text{bulk}} = 0$ (blue), $\lambda_{\text{ave}} = 0$ (green), and $\lambda_{\text{mem}} = 0$ (orange curves, respectively). λ_{mem} is considered only in the domain where $\tau_{\text{mem}} > 0.95$. In (a), two parameters are varied (axes), while the third parameter (title) is kept fixed. In (b), the third parameter is optimized for each combination of the two parameters that are being varied. CV = 4 in all cases shown. (c) The maximal value of α_S for each value of n (x-axis) and CV (color coded). (Parameters σ and θ are optimized for each combination of n and CV.) (d) The maximal value of α_S for each value of σ (x-axis) and CV (color coded as in c). (Parameters n and θ are optimized for each combination of n and CV.)

pressions similar to Eq. 22 with appropriate assumptions, should allow the analysis of the optimal solution's spectrum and its stability in this broad range of problems.

This work was supported by the Wellcome Trust (Investigator Award in Science 212262/Z/18/Z to M.L.), the Human Frontiers Science Programme (Research Grant RGP0044/2018 to M.L.), and the Blavatnik Cambridge Postdoctoral Fellowships (to U.C.). We thank Alessandro Treves and Yasser Roudi for useful discussions.

DETAILS

Simulation results for sparse patterns. For sparse patterns with sparseness $f \in (0, 1]$, a fraction $1 - f$ of the pattern is exactly zero while the rest is log-normal distributed with a mean of 1 and is parametrized by its coefficient of variation (CV, Fig. S1a). For these patterns, the relevant activation function has $\sigma = 0$, and is parametrized by its exponent n (Fig. S1b). In this case, there is no closed-form expression for the optimal solution to Eq. 4, but it can be found numerically using off-the-shelf tools [20]. The resulting weights matrix row sum and L2-norm match the prediction of the replica theory very well (Fig. S1c-d). The maximal number of patterns which can be stored α_C depends only on f , not on other parameters n , θ , CV or N (Fig. S1e-f) and scales asymptotically as $1/f \log(1/f)$, as in [12] (Fig. S1g).

To quantify stability, we define the spectral abscissa as the median, over the stored patterns, of the eigenvalue with the largest real value. Optimizing the threshold θ for pattern stability (e.g., using a line search or finite differentiation with respect to the spectral abscissa), there is an evident stability phase transition at a critical load α_S which increases with sparseness f (Fig. S2a, compare with Fig. S1e), with the transition becoming steeper with N (Fig. S2b, compare with Fig. S1f). For dense patterns, $f = 1$, no memory pattern is stable, in agreement with the limit $\sigma \rightarrow 0$ extrapolated from Fig. 3a-b (left column). The optimal threshold (empirically found) is always negative (Fig. S2c), as well as the resulting weights sum at the optimal threshold (Fig. S1c), and the spectral abscissa increases monotonically with the load (Fig. S2d).

Unlike the critical load for storage (or ‘storage capacity’) α_C , which depends only on f , the critical load for stability α_S depends also on pattern statistics CV and activation function exponent n (at the optimal threshold θ). Interestingly, at low levels of pattern variation $CV \leq 1$ the optimal exponent is sublinear $n^* < 1$, while for high levels of pattern variation $CV \geq 1$ the optimal exponent is linear, $n^* \approx 1$ (Fig. S2e). Thus, for binary patterns where $CV = 0$, $n^* \approx 0$ is optimal, as was the choice in [Hopfield (1982)] [1]. On the other hand, for high-variance patterns, we predict an optimal $n^* \approx 1$.

Measures of non-normal dynamics. The asymmetry index is defined as $\|\mathbf{W}_{\text{asym}}\|_F / (\|\mathbf{W}_{\text{sym}}\|_F + \|\mathbf{W}_{\text{asym}}\|_F)$

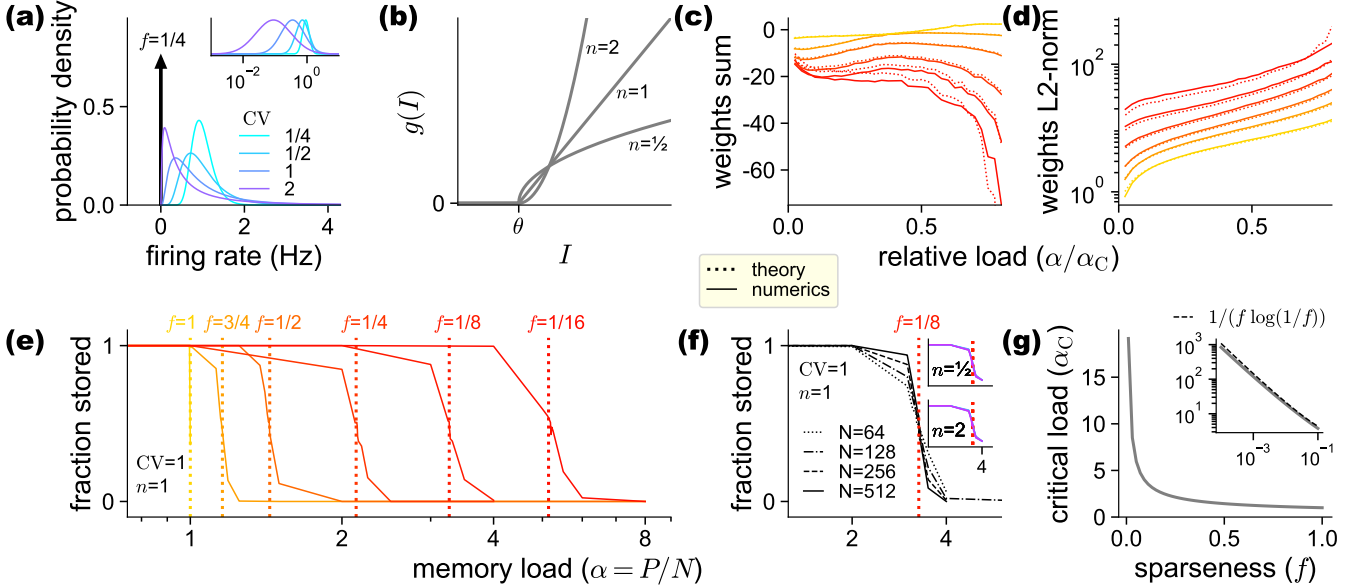


FIG. S1. Capacity phase-transition for sparse patterns. (a) Probability density of sparse, log-normal distributed patterns at different variation levels (CV, color coded). A fraction $1 - f$ of the density is exactly at 0 (arrow). The inset shows normalized density on a log scale. (b) Rectified power activation with threshold θ and different exponents n . (c,d) Weights matrix row sum (c) and L2-norm (d) at different sparseness levels (color coded; empirical - full line, theory - dotted line) and loads (x-axis). (e-f) The fraction of patterns that are correctly stored in simulations (full line) at different loads (x-axis), and different sparseness levels (e, color coded), or different values of N (f, see legend), or different values of n and CV (f, insets). Theory's predictions on the critical load - dotted lines. (g) The relation between f and α_C in linear scale or log-log scale (inset).

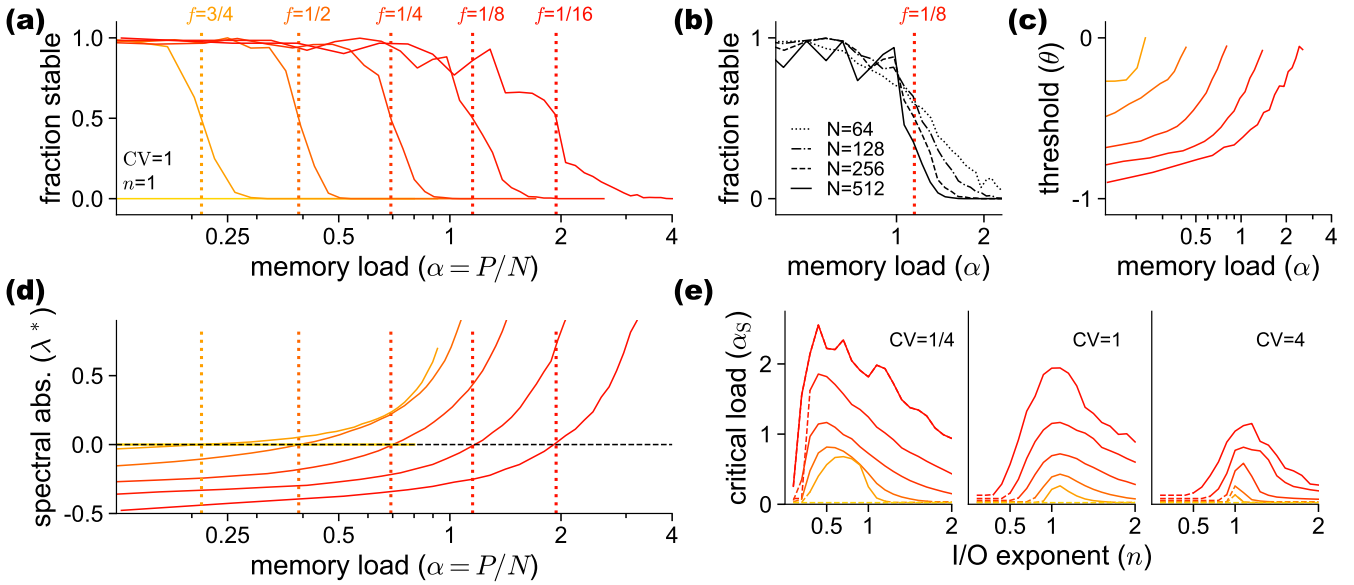


FIG. S2. Stability phase-transition for sparse patterns. (a-b) The fraction of patterns which are stable for recall in simulations (full line) at different loads (x-axis), and different sparseness levels (a, color coded), or different values of N (b, see legend). The empirically found critical load α_S - dotted lines. (c-d) The optimal choice for threshold θ (c) and mean spectral abscissa λ^* (the real part of the eigenvalue with the largest real part) (d) at different loads (x-axis), and different sparseness levels (color coded), for the same experiments as a. (e) The empirically found critical load for stability α_S at different levels of variation (panels), different I/O exponents (x-axis), and levels of sparseness (color coded). Dashed lines connect load values below the minimal value identifiable by the experiments.

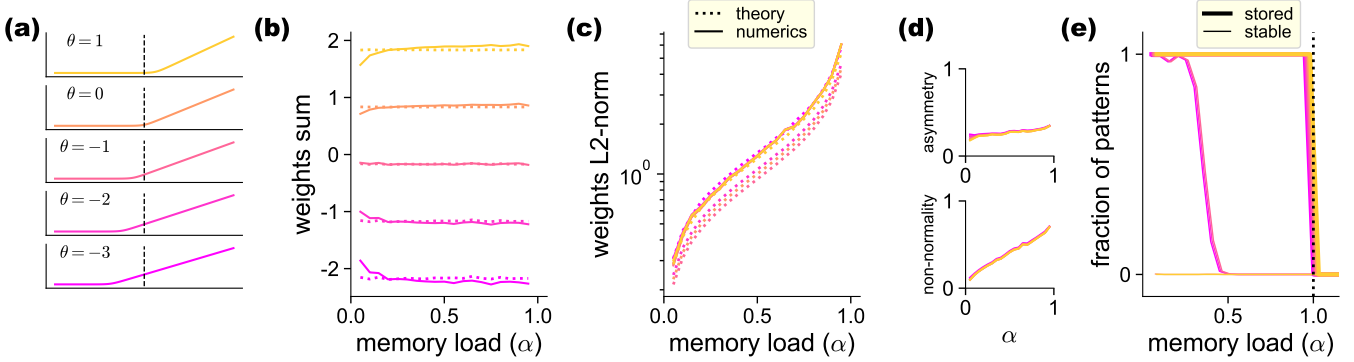


FIG. S3. **Storing fixed-points.** (a) The activation function for different choices of the threshold θ (color coded), with $\sigma = 1, n = 1$. (b-e) Same as Fig. 1b-e for different values of the threshold θ (colors and parameters as in a) with $CV = 2$.

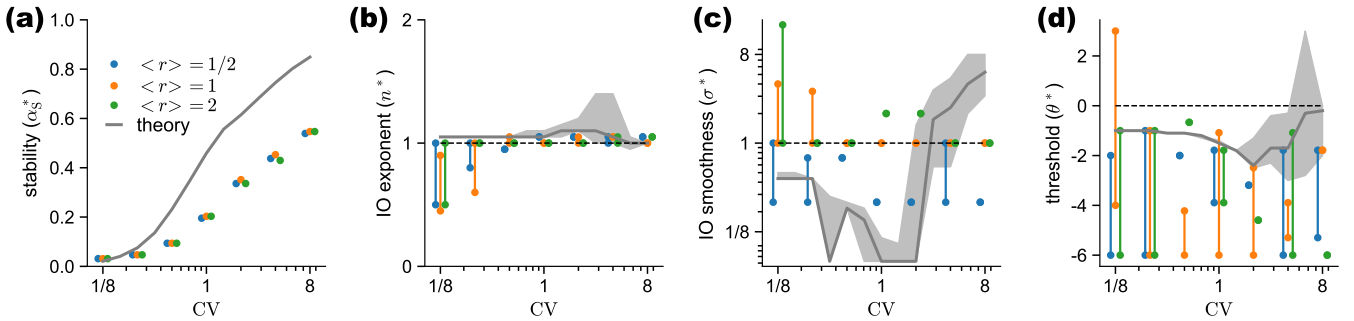


FIG. S4. **Optimal parameters.** (a) The critical load for stability using optimal parameters, at different pattern variation levels (x-axis), per theory (gray line) or simulations with different choices of $\langle r \rangle$ (dots). (b-d) The optimal values (achieving α_S^* in a) of I/O smoothness (b), I/O exponent (c), and threshold (d) at different pattern variation levels (x-axis), color-coded as in a. The range of values achieving 97.5% of the optimum is indicated by a vertical line (simulations) and shading (theory).

using the symmetric and anti-symmetric parts of the weights $\mathbf{W} = \mathbf{W}_{\text{sym}} + \mathbf{W}_{\text{asym}}$. The non-normality index is Henrici's deviation from normality index [51, 52] for the Jacobian \mathbf{J} , $\sqrt{\|\mathbf{J}\|_F^2 - \sum_i |\lambda_i|^2} / \|\mathbf{J}\|_F$, where $\{\lambda_i\}_{i=1}^N$ are the Jacobian eigenvalues.

Optimal dense patterns. In the dense case, Eq. 4 can be solved in closed-form by denoting a Lagrangian:

$$\mathcal{L} = \frac{1}{2} \text{Tr} \mathbf{W}^T \mathbf{W} + \text{Tr} [\boldsymbol{\Gamma}^T (\mathbf{V} - \mathbf{W} \mathbf{R})] + \boldsymbol{\gamma}^T \text{diag}(\mathbf{W})$$

where $\mathbf{R}, \mathbf{V} \in \mathbb{R}^{N \times P}$ as defined in the main text, $\boldsymbol{\Gamma} \in \mathbb{R}^{N \times P}$ are Lagrange multipliers enforcing the fixed-points and $\boldsymbol{\gamma} \in \mathbb{R}^N$ are Lagrange multipliers enforcing lack of self-coupling in the connectivity. Then the optimal weights satisfy $0 = \frac{\partial \mathcal{L}}{\partial \mathbf{W}}$, $0 = \mathbf{V} - \mathbf{W} \mathbf{R}$, and $0 = \text{diag}(\mathbf{W})$, which we solve for $\boldsymbol{\Gamma}$:

$$\begin{aligned} \mathbf{W} &= \boldsymbol{\Gamma} \mathbf{R}^T - \boldsymbol{\gamma} \circ \mathbf{I} \\ \mathbf{V} &= \mathbf{W} \mathbf{R} = \boldsymbol{\Gamma} \mathbf{R}^T \mathbf{R} - \boldsymbol{\gamma} \circ \mathbf{R} \\ \boldsymbol{\Gamma} &= \mathbf{V} (\mathbf{R}^T \mathbf{R})^{-1} + \boldsymbol{\gamma} \circ \mathbf{R} (\mathbf{R}^T \mathbf{R})^{-1} \end{aligned}$$

so that substituting $\boldsymbol{\Gamma}$ we have an expression for \mathbf{W} in terms of the pseudo-inverse $\mathbf{R}^\dagger = (\mathbf{R}^T \mathbf{R})^{-1} \mathbf{R}^T$:

$$\mathbf{W} = \mathbf{V} \mathbf{R}^\dagger - \boldsymbol{\gamma} \circ (\mathbf{I}_N - \mathbf{R} \mathbf{R}^\dagger) \quad (19)$$

and γ_i is given by the equation $W_{ii} = 0$:

$$\gamma_i = [\mathbf{V} \mathbf{R}^\dagger]_{ii} / [\mathbf{I}_N - \mathbf{R} \mathbf{R}^\dagger]_{ii}$$

Finally, without avoiding self-coupling in the connectivity \mathbf{W} , we have $\boldsymbol{\gamma} = 0$ and recover Eq. 8.

Stability transition in paired Gaussian matrices. As we previously showed [22], for a pair of rectangular matrices $\mathbf{X}, \mathbf{Y} \in \mathbb{R}^{N \times P}$ for $\alpha = P/N < 1$, whose corresponding entries are jointly Gaussian, i.e., any $(x, y) = (X_{i\mu}, Y_{i\mu})$ are i.i.d. $(x, y) \sim \mathcal{N} \left(0, \begin{pmatrix} \sigma_x^2 & \tau \sigma_x \sigma_y \\ \tau \sigma_x \sigma_y & \sigma_y^2 \end{pmatrix} \right)$, the support of the eigenvalue spectrum of $\mathbf{M} = \mathbf{X} \mathbf{Y}^\dagger$ for $N, P \rightarrow \infty$ is given by a circular law:

$$\left| \lambda - \tau \frac{\sigma_x}{\sigma_y} \right|^2 \leq \frac{\sigma_x^2}{\sigma_y^2} (1 - \tau^2) \frac{\alpha}{1 - \alpha} \quad (20)$$

which is quite precise already for moderate N (Fig. S5).

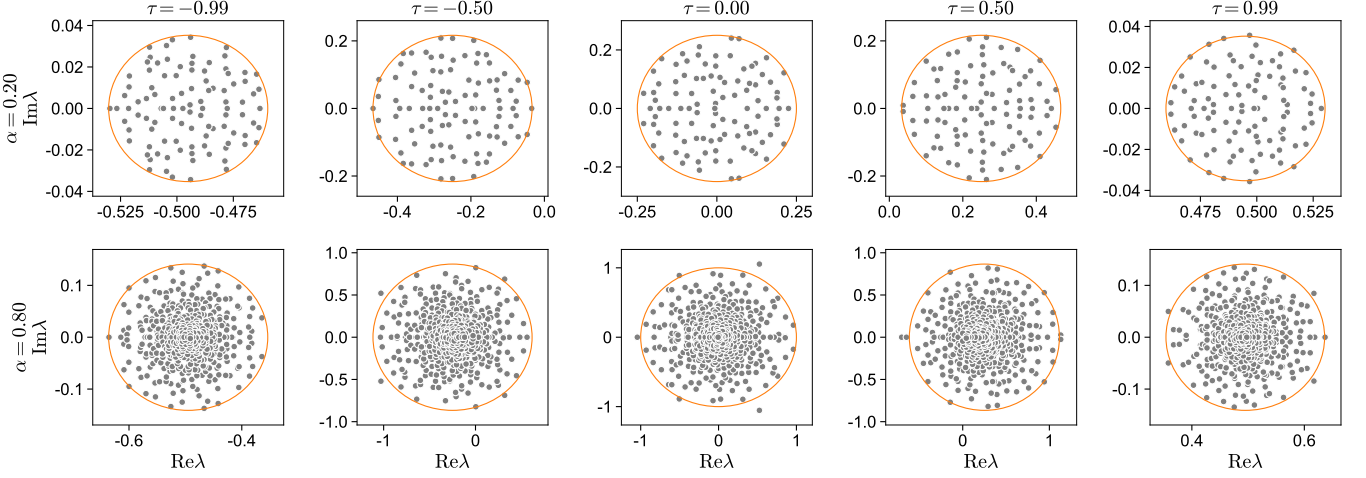


FIG. S5. **Eigenvalue spectrum of the Gaussian pseudo-inverse ensemble, $\mathbf{M} = \mathbf{X} \mathbf{Y}^\dagger$.** Eigenvalues (gray dots) and predicted support (orange contour, Eq. 20) at different values of α (rows) and τ (columns). We used $N = 500$, $\sigma_x = 1$, $\sigma_y = 2$. Note the difference between panels in the range of the axes, as predicted by theory.

As a corollary, for $\mathbf{M} = -c\mathbf{I} + \mathbf{X} \mathbf{Y}^\dagger$, the upper and lower bounds of $\text{Re}\lambda$ are achieved at real numbers λ_\pm :

$$\lambda_\pm = -c + \frac{\sigma_x}{\sigma_y} \left(\tau \pm \sqrt{\frac{\alpha}{1-\alpha}} \sqrt{1-\tau^2} \right) \quad (21)$$

yielding Eq. 10 in the main text where λ_+ is called λ_{bulk} .

Noting that $\alpha/(1-\alpha)$ is strictly monotonic for $\alpha \in (0, 1)$, we can denote by α_S the largest α where $\lambda_+ < 0$, $\alpha_S = \max_{\lambda_+(\alpha) < 0} \alpha$, and solve from the condition $\lambda_+ < 0$:

$$\begin{aligned} \sqrt{\frac{\alpha}{1-\alpha}} &< \frac{c\sigma_y^2 - \tau\sigma_x\sigma_y}{\sigma_x\sigma_y\sqrt{1-\tau^2}} \\ \alpha &< \frac{(c\sigma_y^2 - \tau\sigma_x\sigma_y)^2}{\sigma_x^2\sigma_y^2(1-\tau^2) + (c\sigma_y^2 - \tau\sigma_x\sigma_y)^2} \end{aligned}$$

so that when $c\sigma_y^2 - \tau\sigma_x\sigma_y < 0$ this inequality does not have a solution, and we can express α_S compactly as

$$\alpha_S = \frac{\max(0, c\sigma_y^2 - \tau\sigma_x\sigma_y)^2}{\sigma_x^2\sigma_y^2(1-\tau^2) + (c\sigma_y^2 - \tau\sigma_x\sigma_y)^2} \quad (22)$$

and Eq. 11 in the main text follows for $c = 1$.

Stability dependence on the threshold. In Eq. 11, α_S^{bulk} dependence on σ , n , and θ is hidden within the three (co)variance terms and is, in general, complex. Less so for θ : c_{rr} do not include θ at all, and furthermore c_{rf} is independent of θ because $c_{\text{rf}} = \langle \delta r \delta g'(g^{-1}(r')) g^{-1}(r) \rangle + \theta \langle \delta r \delta g'(g^{-1}(r')) \rangle$, where the right term is 0 due to the independence of r, r' . As c_{ff} depends on θ , so does α_S^{bulk} , but the condition $\alpha_S^{\text{bulk}} > 0$ which depends only on the numerator of Eq. 11, or $c_{\text{rr}} > c_{\text{rf}}$, is independent of θ .

The zero crossing of λ_{ave} and λ_{mem} are expressed in Eqs. 17 and 18, respectively. The former is derived from

Eq. 12, and the latter from Eq. 15 by noting that $c_{\text{rf}} = \langle \delta r \delta g'(g^{-1}(r)) g^{-1}(r) \rangle + \theta \langle \delta r \delta g'(g^{-1}(r)) \rangle$.

An outlier related to the Jacobian average value. To empirically find the outlier related to the Jacobian average value, we note that if all the eigenvectors were real, this outlier would have been associated with the eigenvector of \mathbf{J} closest to the uniform vector $\mathbf{1}$:

$$v_{\text{ave}} = \arg \max_{v \in \{\text{EV}(\mathbf{J}): \|v\|=1\}} \mathbf{1}^T v \quad (23)$$

Generalizing this idea to complex eigenvectors, we find the eigenvector v such that the projection of the uniform vector $\mathbf{1}$ onto the span of $\text{Re}(v), \text{Im}(v)$ is of maximal norm. Denoting $V = [\text{Re}(v), \text{Im}(v)] \in \mathbb{R}^{N \times 2}$ we have:

$$v_{\text{ave}} = \arg \max_{v \in \{\text{EV}(\mathbf{J}): \|v\|=1\}} \mathbf{1}^T V V^+ \mathbf{1} \quad (24)$$

where V^+ denotes the Moore-Penrose pseudo-inverse. Then $\lambda_{\text{ave}}^{\text{emp}}$ is the eigenvalue associated with v_{ave} .

An outlier related to the memory pattern. When for some constant c , $\mathbf{r}^\mu + c\mathbf{1}$ is an eigenvector of the Jacobian J^μ (Eq. 5) with eigenvalue λ_{mem} :

$$\lambda_{\text{mem}}(\mathbf{r}^\mu + c\mathbf{1}) = -\mathbf{r}^\mu + \mathbf{g}'(\mathbf{g}^{-1}(\mathbf{r}^\mu)) \circ \mathbf{W} \mathbf{r}^\mu + c\lambda_{\text{ave}}$$

so denoting $\phi(x) = \mathbf{g}'(\mathbf{g}^{-1}(x)) \circ (\mathbf{g}^{-1}(x) + \theta)$ we have

$$(\lambda_{\text{mem}} + 1)\mathbf{r}^\mu + \lambda_{\text{mem}}c\mathbf{1} = \phi(\mathbf{r}^\mu) + c\lambda_{\text{ave}}\mathbf{1}$$

a linear relation between \mathbf{r}^μ and $\phi(\mathbf{r}^\mu)$, characterized by a Pearson correlation close to 1, Eq. 14, and in this case $\lambda_{\text{mem}} + 1$ is given by the linear regression slope, Eq. 15.

Code availability. All code used to generate the included figures will be made public upon publication and is available upon request from the corresponding author.

* corresponding author: uc231@cam.ac.uk

[1] J. J. Hopfield, Neural networks and physical systems with emergent collective computational abilities., *Proceedings of the national academy of sciences* **79**, 2554 (1982).

[2] D. J. Amit, H. Gutfreund, and H. Sompolinsky, Spin-glass models of neural networks, *Physical Review A* **32**, 1007 (1985).

[3] I. Kanter and H. Sompolinsky, Associative recall of memory without errors, *Physical Review A* **35**, 380 (1987).

[4] M. Tsodyks, Associative memory in asymmetric diluted network with low level of activity, *Europhysics Letters* **7**, 203 (1988).

[5] A. Treves, Graded-response neurons and information encodings in autoassociative memories, *Physical Review A* **42**, 2418 (1990).

[6] M. Lengyel, J. Kwag, O. Paulsen, and P. Dayan, Matching storage and recall: hippocampal spike timing-dependent plasticity and phase response curves, *Nature neuroscience* **8**, 1677 (2005).

[7] D. Krotov and J. J. Hopfield, Dense associative memory for pattern recognition, *Advances in neural information processing systems* **29** (2016).

[8] R. Kree and A. Zippelius, Continuous-time dynamics of asymmetrically diluted neural networks, *Physical Review A* **36**, 4421 (1987).

[9] A. Treves and D. J. Amit, Metastable states in asymmetrically diluted hopfield networks, *Journal of Physics A: Mathematical and General* **21**, 3155 (1988).

[10] B. Tirozzi and M. Tsodyks, Chaos in highly diluted neural networks, *Europhysics Letters* **14**, 727 (1991).

[11] E. Gardner, The space of interactions in neural network models, *Journal of physics A: Mathematical and general* **21**, 257 (1988).

[12] F. Schönsberg, Y. Roudi, and A. Treves, Efficiency of local learning rules in threshold-linear associative networks, *Physical Review Letters* **126**, 018301 (2021).

[13] D. Festa, G. Hennequin, and M. Lengyel, Analog memories in a balanced rate-based network of EI neurons, in *Advances in Neural Information Processing Systems* (2014) pp. 2231–2239.

[14] A. Treves and E. T. Rolls, Computational constraints suggest the need for two distinct input systems to the hippocampal ca3 network, *Hippocampus* **2**, 189 (1992).

[15] A. Treves, W. E. Skaggs, and C. A. Barnes, How much of the hippocampus can be explained by functional constraints?, *Hippocampus* **6**, 666 (1996).

[16] K. D. Miller and F. Fumarola, Mathematical equivalence of two common forms of firing rate models of neural networks, *Neural computation* **24**, 25 (2012).

[17] M. Khona and I. R. Fiete, Attractor and integrator networks in the brain, *Nature Reviews Neuroscience* **23**, 744 (2022).

[18] U. Cohen and H. Sompolinsky, Soft-margin classification of object manifolds, *Physical Review E* **106**, 024126 (2022).

[19] M. Mézard, G. Parisi, and M. A. Virasoro, *Spin glass theory and beyond: An Introduction to the Replica Method and Its Applications*, Vol. 9 (World Scientific Publishing Company, 1987).

[20] P. J. Goulart and Y. Chen, Clarabel: An interior-point solver for conic programs with quadratic objectives (2024), arXiv:2405.12762 [math.OC].

[21] L. Personnaz, I. Guyon, and G. Dreyfus, Information storage and retrieval in spin-glass like neural networks, *Journal de Physique Lettres* **46**, 359 (1985).

[22] U. Cohen, Eigenvalue spectrum support of paired random matrices with pseudo-inverse, arXiv preprint arXiv:2506.21244 (2025).

[23] B. Willmore and D. J. Tolhurst, Characterizing the sparseness of neural codes, *Network: Computation in Neural Systems* **12**, 255 (2001).

[24] B. A. Olshausen and D. J. Field, Sparse coding of sensory inputs, *Current opinion in neurobiology* **14**, 481 (2004).

[25] S. R. Dubey, S. K. Singh, and B. B. Chaudhuri, Activation functions in deep learning: A comprehensive survey and benchmark, *Neurocomputing* **503**, 92 (2022).

[26] D. Rubin, S. van Hooser, and K. Miller, The stabilized supralinear network: a unifying circuit motif underlying multi-input integration in sensory cortex, *Neuron* **85**, 402 (2015).

[27] Y. Ahmadian and K. D. Miller, What is the dynamical regime of cerebral cortex?, *Neuron* **109**, 3373 (2021).

[28] D. Golomb, N. Rubin, and H. Sompolinsky, Willshaw model: Associative memory with sparse coding and low firing rates, *Physical Review A* **41**, 1843 (1990).

[29] R. M. May, Will a large complex system be stable?, *Nature* **238**, 413 (1972).

[30] H. J. Sommers, A. Crisanti, H. Sompolinsky, and Y. Stein, Spectrum of large random asymmetric matrices, *Physical review letters* **60**, 1895 (1988).

[31] T. Guhr, A. Müller-Groeling, and H. A. Weidenmüller, Random-matrix theories in quantum physics: common concepts, *Physics Reports* **299**, 189 (1998).

[32] M. L. Mehta, *Random matrices* (Elsevier, 2004).

[33] Z. Bai and J. W. Silverstein, *Spectral analysis of large dimensional random matrices*, Vol. 20 (Springer, 2010).

[34] M. Stern, H. Sompolinsky, and L. F. Abbott, Dynamics of random neural networks with bistable units, *Physical Review E* **90**, 062710 (2014).

[35] Y. Ahmadian, F. Fumarola, and K. D. Miller, Properties of networks with partially structured and partially random connectivity, *Physical Review E* **91**, 012820 (2015).

[36] L. Poley, T. Galla, and J. W. Baron, Eigenvalue spectra of finely structured random matrices, *Physical Review E* **109**, 064301 (2024).

[37] T. Tao, V. Vu, and M. Krishnapur, Random matrices: Universality of esds and the circular law (2009), arXiv:0807.4898 [math.PR].

[38] H. Sompolinsky, A. Crisanti, and H.-J. Sommers, Chaos in random neural networks, *Physical review letters* **61**, 259 (1988).

[39] J. Kadmon and H. Sompolinsky, Transition to chaos in random neuronal networks, *Physical Review X* **5**, 041030 (2015).

[40] Y. V. Fyodorov and B. A. Khoruzhenko, Nonlinear analogue of the may-wigner instability transition, *Proceedings of the National Academy of Sciences* **113**, 6827 (2016).

[41] G. Wainrib and J. Touboul, Topological and dynamical complexity of random neural networks, *Physical review letters* **110**, 118101 (2013).

[42] G. Ben Arous, Y. V. Fyodorov, and B. A. Khoruzhenko, Counting equilibria of large complex systems by instability index, *Proceedings of the National Academy of Sciences* **118**, e2023719118 (2021).

- [43] S. O'Rourke and D. Renfrew, Low rank perturbations of large elliptic random matrices, *Electron. J. Probab* **19**, 1 (2014).
- [44] F. Mastrogiovanni and S. Ostoja, Linking connectivity, dynamics, and computations in low-rank recurrent neural networks, *Neuron* **99**, 609 (2018).
- [45] A. Rivkind and O. Barak, Local dynamics in trained recurrent neural networks, *Physical review letters* **118**, 258101 (2017).
- [46] F. Schuessler, A. Dubreuil, F. Mastrogiovanni, S. Ostoja, and O. Barak, Dynamics of random recurrent networks with correlated low-rank structure, *Physical Review Research* **2**, 013111 (2020).
- [47] D. S. Broomhead and G. P. King, Extracting qualitative dynamics from experimental data, *Physica D: Nonlinear Phenomena* **20**, 217 (1986).
- [48] N. Golyandina, V. Nekrutkin, and A. A. Zhigljavsky, *Analysis of time series structure: SSA and related techniques* (CRC press, 2001).
- [49] H. Martens and T. Næs, *Multivariate calibration* (John Wiley & Sons, 1992).
- [50] P. J. Schmid, Dynamic mode decomposition and its variants, *Annual Review of Fluid Mechanics* **54**, 225 (2022).
- [51] P. Henrici, Bounds for iterates, inverses, spectral variation and fields of values of non-normal matrices, *Numerische Mathematik* **4**, 24 (1962).
- [52] L. N. Trefethen and M. Embree, *Spectra and pseudospectra: the behavior of nonnormal matrices and operators* (Princeton university press, 2020).

APPENDIX

Mean-field theory for the number of achievable fixed points. We consider P graded patterns $\mathbf{r}^\mu \in \mathbb{R}_+^N$ for $\mu = 1 \dots P$, with sparseness level of $f \in (0, 1]$, so that a fraction $1 - f$ of all entries are exactly 0. We develop a replica theory for the ability to satisfy the P non-linear equations $\mathbf{g}(\mathbf{W}\mathbf{r}^\mu - \theta) = \mathbf{r}^\mu$, defining P fixed-points for the dynamics of Eq. 1, for a scalar θ and an activation function $g(\cdot)$. As the problem decouples for different rows, we denote the volume of solutions for a single row $\mathbf{w} = \mathbf{w}^k$ of the matrix \mathbf{W} , for any $k = 1 \dots N$:

$$\mathcal{V} = \{\mathbf{w} : (r_k^\mu > 0 \cap \mathbf{w}^\top \mathbf{r}^\mu = \theta + g^{-1}(r_k^\mu)) \cup (r_k^\mu = 0 \cap \mathbf{w}^\top \mathbf{r}^\mu \leq \theta)\} \quad (25)$$

This framing captures both the dense case where $f = 1$ and the activation is strictly monotonic $g(\cdot) : \mathbb{R} \rightarrow \mathbb{R}_+$, and the sparse case where we assume that the activation is rectified, i.e., $g(\cdot) : \mathbb{R}_+ \rightarrow \mathbb{R}_+$ is strictly monotonic with $g(0) = 0$ and define $g(x) = 0$ for any $x < 0$. The notation $g^{-1}(\cdot)$ is defined only where $g(\cdot)$ is strictly monotonic.

By characterising the conditions where the volume of solutions V vanishes, and correlation between different solutions peaks, we capture the unique minimal-norm solution corresponding to Eq. 4 in any finite $\alpha = P/N$. Intuitively, in this regime, only a single weight matrix solves the equations. As usual, it is sufficient to find G^* such that $[V^n] = e^{nG^*}$ as invoking the replica identify $[\log V] = \lim_{n \rightarrow 0} \frac{1}{n} ([V^n] - 1)$ and L'Hôpital's rule implies $[\log V] = G^*$.

We start by writing the replicated volume in terms of Dirac δ , Kronecker δ , and the Heaviside step function Θ :

$$V^n = \int d^{N \times n} w_i^\alpha \prod_{\alpha}^n \prod_{\mu}^P \left(\left(1 - \delta_{r_k^\mu} \right) \delta \left(\theta + g^{-1}(r_k^\mu) - \sum_i^N w_i^\alpha r_i^\mu \right) + \delta_{r_k^\mu} \Theta \left(\theta - \sum_i^N w_i^\alpha r_i^\mu \right) \right)$$

which we seek to average it over the i.i.d. sampling of the patterns r_i^μ , noting it can be done independently assuming there are no self-couplings $W_{kk} = w_k = 0$ so that terms with r_i^μ and r_k^μ are independent. We denote:

$$\begin{aligned} I_1 &= \left[\left[\prod_{\alpha}^n \delta \left(\theta + g^{-1}(r_k^\mu) - \sum_i^N w_i^\alpha r_i^\mu \right) \right]_{r^\mu} \right]_{r_k^\mu > 0} \\ I_2 &= \left[\prod_{\alpha}^n \Theta \left(\theta - \sum_i^N w_i^\alpha r_i^\mu \right) \right]_{r^\mu} \end{aligned}$$

and use the Taylor expansion of $[e^x]$ around $[x]$, $[e^x] \approx e^{[x] + \frac{1}{2}[(\delta x)^2]}$, denoting the pattern statistics $x_1 = [r_i^\mu]$, $x_2 = [(\delta r_i^\mu)^2]$, $y_1 = [g^{-1}(r_k^\mu) | r_k^\mu > 0]$, $y_2 = [(\delta g^{-1}(r_k^\mu))^2 | r_k^\mu > 0]$, and using the independence $[\delta r_i^\mu \delta r_j^\mu] = \delta_{ij} x_2$:

$$\begin{aligned} I_1 &= \int d^n \hat{s}^\alpha e^{i \sum_{\alpha}^n \hat{s}^\alpha (\theta + y_1 - x_1 m^\alpha) - \frac{1}{2} \sum_{\alpha\beta}^n \hat{s}^\alpha \hat{s}^\beta (x_2 Q_{\alpha\beta} + y_2)} \\ I_2 &= \int_{-\infty}^{\theta} d^n h_\alpha \int d^n \hat{s}^\alpha e^{i \sum_{\alpha}^n \hat{s}^\alpha (x_1 m^\alpha - h_\alpha) - \frac{1}{2} \sum_{\alpha\beta}^n \hat{s}^\alpha \hat{s}^\beta (x_2 Q_{\alpha\beta})} \end{aligned}$$

denoting new order parameters for the weight correlations, $m^\alpha = \sum_i^N w_i^\alpha$ and $Q_{\alpha\beta} = \sum_i^N w_i^\alpha w_i^\beta$ (note the different scaling compared to [12]). After N decoupled n -dimensions Gaussian integrals on w_i^α we have:

$$\begin{aligned} [V^n]_r &= \int d^n m_\alpha \int \frac{d^n \hat{m}_\alpha}{2\pi} \int d^{n \times n} Q_{\alpha\beta} \int \frac{d^{n \times n} \hat{Q}_{\alpha\beta}}{2\pi} e^{N G} \\ G &= \frac{1}{N} \sum_{\alpha}^n i \hat{m}_\alpha m_\alpha + \frac{1}{2N} \sum_{\alpha\beta}^n (2i \hat{Q}_{\alpha\beta}) Q_{\alpha\beta} - \frac{1}{2} \log \det (2i \hat{Q}) \\ &\quad + \frac{1}{2} \sum_{\alpha\beta}^n i \hat{m}_\alpha i \hat{m}_\beta (\hat{Q}_{\alpha\beta})^{-1} + f \alpha \log I_1 + (1 - f) \alpha \log I_2 \end{aligned}$$

Assuming the replica symmetry ansatz $m_\alpha = m$, $i \hat{m}_\alpha = \hat{m}$, $Q_{\alpha\beta} = q + (q_0 - q) \delta_{\alpha\beta}$ and $2i \hat{Q}_{\alpha\beta} = \hat{q} + (\hat{q}_0 - \hat{q}) \delta_{\alpha\beta}$:

$$\begin{aligned} [V^n]_r &= \int dm \int d\hat{m} \int dq_0 \int dq \int d\hat{q}_0 \int d\hat{q} e^{N n G} \\ G &= \frac{1}{N} \hat{m} m + \frac{1}{2N} (q_0 \hat{q}_0 - q \hat{q}) - \frac{1}{2} \log (\hat{q}_0 - \hat{q}) - \frac{1}{2} \frac{\hat{q}}{\hat{q}_0 - \hat{q}} + \frac{1}{2} \frac{\hat{m}^2}{\hat{q}_0 - \hat{q}} + \frac{f\alpha}{n} \log I_1 + \frac{(1 - f)\alpha}{n} \log I_2 \end{aligned}$$

Now using Hubbard-Stratonovich $e^{-y^2/2} = \int Dte^{ity}$ for $Dt = \frac{dt}{\sqrt{2\pi}}e^{-t^2/2}$ to get rid of the squares and decouple the n replicas, I_1, I_2 become:

$$\begin{aligned} I_1 &= \int d^n \hat{s}^\alpha e^{i \sum_\alpha \hat{s}^\alpha (\theta + y_1 - x_1 m) - \frac{1}{2} x_2 (q_0 - q) \sum_\alpha (\hat{s}^\alpha)^2 - \frac{1}{2} (\sqrt{x_2 q} + y_2) \sum_\alpha \hat{s}^\alpha)^2} \\ &= \int Dt \left(e^{-\frac{1}{2} \frac{(\theta + y_1 - x_1 m + t \sqrt{x_2 q} + y_2)^2}{x_2 (q_0 - q)} - \frac{1}{2} \log(x_2 (q_0 - q))} \right)^n \\ I_2 &= \int_{-\infty}^{\theta} d^n h_\alpha \int d^n \hat{s}^\alpha e^{i \sum_\alpha \hat{s}^\alpha (x_1 m^\alpha - h_\alpha) - \frac{1}{2} x_2 (q_0 - q) \sum_\alpha (\hat{s}^\alpha)^2 - \frac{1}{2} (\sqrt{x_2 q} \sum_\alpha \hat{s}^\alpha)^2} \\ &= \int Dt \left(\int_{-\infty}^{\theta} dh e^{-\frac{1}{2} \frac{(x_1 m - h + t \sqrt{x_2 q})^2}{x_2 (q_0 - q)} - \frac{1}{2} \log(x_2 (q_0 - q))} \right)^n \end{aligned}$$

and using the replica trick $\log \int Dt (Z(t))^n = n \int Dt \log Z(t)$ for $n \rightarrow 0$ we have:

$$\begin{aligned} \log I_1 &= -\frac{n}{2} \left(\frac{(\theta + y_1 - x_1 m)^2}{x_2 (q_0 - q)} + \frac{x_2 q + y_2}{x_2 (q_0 - q)} + \log(x_2 (q_0 - q)) \right) \\ \log I_2 &= n \int Dt \log \int_{-\infty}^{\theta} dh e^{-\frac{1}{2} \frac{(x_1 m - h + t \sqrt{x_2 q})^2}{x_2 (q_0 - q)} - \frac{1}{2} \log x_2 (q_0 - q)} \end{aligned}$$

Taking the limit $N \rightarrow \infty$ we consider the saddle-point equations $0 = \frac{\partial G}{\partial \hat{m}} = \frac{\partial G}{\partial \hat{q}} = \frac{\partial G}{\partial \hat{q}_0}$ which are solved for:

$$G^* = \frac{1}{2} - \frac{1}{2} \frac{m^2/N}{q_0 - q} + \frac{1}{2} \log(q_0 - q) + \frac{1}{2} \frac{q}{q_0 - q} + \frac{\alpha f}{n} \log I_1 + \frac{\alpha(1-f)}{n} \log I_2$$

As we aim to recover the minimal norm weights, we are interested in the limit where the volume vanishes and only a single solution remains, which is captured by the limit $0 = \lim_{q_0 \rightarrow q} (q_0 \rightarrow q) G^*$, defining $\theta_0 = \frac{\theta - x_1 m}{\sqrt{x_2 q}}$ for short:

$$\begin{aligned} \lim_{q_0 \rightarrow q} (q_0 - q) \frac{1}{n} \log I_1 &= -\frac{1}{2} \left(\left(\frac{y_1}{\sqrt{x_2}} + \frac{\theta - x_1 m}{\sqrt{x_2}} \right)^2 + q + \frac{y_2}{x_2} \right) \\ \lim_{q_0 \rightarrow q} (q_0 - q) \frac{1}{n} \log I_2 &= -\frac{\alpha q}{2} \int_{\frac{\theta - x_1 m}{\sqrt{x_2 q}}}^{\infty} Dt \left(t - \frac{\theta - x_1 m}{\sqrt{x_2 q}} \right)^2 \\ \lim_{q_0 \rightarrow q} (q_0 - q) G^* &= \frac{q - m^2/N}{2} - f \frac{\alpha q}{2} \left(\theta_0 + \frac{y_1}{\sqrt{x_2 q}} \right)^2 - f \frac{\alpha q}{2} \left(1 + \frac{y_2}{x_2 q} \right) - (1-f) \frac{\alpha q}{2} \int_{\theta_0}^{\infty} Dt (t - \theta_0)^2 \end{aligned}$$

Noting that $m^2/N \ll q$ as $m \sim O(1)$ and substituting $0 = \lim_{q_0 \rightarrow q} (q_0 \rightarrow q) G^*$ we have one equation relating the unknown quantities q, θ_0 through the known quantities $\alpha, x_1, x_2, y_1, y_2$. Assuming the solution is achieved at a finite value of q , it would satisfy a saddle-point with respect to it $0 = \frac{\partial G}{\partial q}$, yielding a second equation. The resulting self-consistent equations become, solving the integral and denoting $h(x) = e^{-x^2/2}/\sqrt{2\pi}$ and $H(x) = \int_x^\infty h(x)$:

$$\begin{aligned} \alpha^{-1} &= f \left(\theta_0 + \frac{y_1}{\sqrt{x_2 q}} \right)^2 + f \left(\frac{y_2}{x_2 q} + 1 \right) + (1-f) ((\theta_0^2 + 1) H(\theta_0) - \theta_0 h(\theta_0)) \\ 0 &= f \left(\theta_0 + \frac{y_1}{\sqrt{x_2 q}} \right) + (1-f) (\theta_0 H(\theta_0) - h(\theta_0)) \\ \theta &= mx_1 + \theta_0 \sqrt{x_2 q} \end{aligned}$$

Those equations are considerably simplified for $f = 1$, yielding Eq. 6-7 for the moments of \mathbf{W} . The equations for the critical storage capacity α_C are given by noting that the weights norm diverges in this case, $q \rightarrow \infty$:

$$\begin{aligned} \alpha_C^{-1} &= f \theta_0^2 + f + (1-f) ((\theta_0^2 + 1) H(\theta_0) - \theta_0 h(\theta_0)) \\ 0 &= f \theta_0 + (1-f) (\theta_0 H(\theta_0) - h(\theta_0)) \end{aligned}$$

which can be solved numerically, first for θ_0 , then for α_C . For the dense case, $f = 1$, we have $\theta_0 = 0$, and $\alpha_C = 1$.